Structural basis for the sheddase function of human meprin β metalloproteinase at the plasma membrane

Joan L. Arolas[1], Claudia Broder[2], Tamara Jefferson[2],

Tibisay Guevera[1], Erwin E. Sterchi[3], Wolfram Bode[4], Walter Stöcker[5], Christoph Becker-Pauly[2] & F. Xavier Gomis-Rüth[1,*]

[1] Proteolysis Lab; Department of Structural Biology; Molecular Biology Institute of Barcelona, CSIC; Barcelona Science Park; Helix Building; c/ Baldiri Reixac, 15-21; E-08028 Barcelona (Spain).

[2] Institute of Biochemistry; Unit for Degradomics of the Protease Web; University of Kiel; Rudolf-Höber-Straße 1; D-24118 Kiel (Germany).

[3] Institute of Biochemistry and Molecular Medicine, University of Berne; Bühlstrasse 28; CH-3012 Berne (Switzerland).

[4] Arbeitsgruppe Proteinaseforschung; Max-Planck-Institute für Biochemie; Am Klopferspitz 18a; D-82152 Planegg-Martinsried (Germany).

[5] Institute of Zoology; Cell and Matrix Biology; Johannes Gutenberg-University; Johannes-von-Müller-Weg 6; D-55128 Mainz (Germany).

* Correspondence: e-mail: fxgr@ibmb.csic.es, phone: (+34) 934 020 186, fax: (+34) 934 034 979.

The authors state they have no competing financial interest.

Running title: Structure, regulation, and function of human meprin β

ABSTRACT

Ectodomain shedding at the cell surface is a major mechanism to regulate the extracellular and circulatory concentration or the activities of signaling proteins at the plasma membrane. Human meprin β is a 145-KDa disulfide-linked homodimeric multi-domain type-I membrane metallopeptidase that sheds membrane-bound cytokines and growth factors, thereby contributing to inflammatory diseases, angiogenesis, and tumor progression. In addition, amyloid precursor protein (APP) is cleaved at the β-secretase site giving rise to amyloidogenic peptides. We have solved the X-ray crystal structure of a major fragment of the meprin β ectoprotein, the first of a multi-domain oligomeric transmembrane sheddase, and of its zymogen. The meprin β dimer displays a compact shape, whose catalytic domain undergoes major rearrangement upon activation, and reveals an exosite and a sugar-rich channel, both of which possibly engage in substrate binding. A plausible structure-derived working mechanism suggests that substrates such as APP are shed close to the plasma membrane surface following an "N-like" chain trace.

INTRODUCTION

Physiological processes in the extracellular milieu and the circulation require finely tuned concentrations of signal molecules such as cytokines, growth factors, receptors, adhesion molecules, and peptidases. Many of these proteins are synthesized as type-I membrane protein variants or precursors consisting of a glycosylated N-terminal ectoprotein, a transmembrane helix, and a C-terminal cytosolic tail. Their localization at the cell surface restricts their field of action to autocrine or juxtacrine processes. However, to act at a distance in paracrine, synaptic, or endocrine events, they have to be released from the plasma membrane into the extracellular space as soluble factors through "protein ectodomain shedding" (1, 2). This entails limited proteolysis and is a major post-translational regulation mechanism that affects 2–4% of the proteins on the cell surface, occurs at or near the plasma membrane (3), and apparently follows a common release mechanism (2). It may also proteolytically inactivate proteins in order to terminate their function on the cell surface (4). Peptidases engaged in such processing are "sheddases" and the most studied transmembrane sheddases are members of the adamalysin/ADAMs (4, 5) and matrix-metalloproteinase (MMP; (6)) families within the metzincin clan of metallopeptidases (MPs; (7-9)). These include ADAM-8, -9,-10,-12, -15, -17, -19, -28, and -33 (1, 4); and membrane-type 1 (MT1)-MMP, MT3-MMP, and MT5-MMP (2, 6, 10). Other confirmed transmembrane sheddases are the aspartic proteinases BACE-1 and -2 (see (11) and references therein), and the malarian parasite serine proteinases, PfSUB2, PfROM1 and PfROM4 (12). Distinct sheddases may participate in intercalating processes, with disparate physiological consequences: ADAM-9, -10 (α-secretases), and -17 contribute to the non-amyloidogenic pathway of human amyloid precursor protein (APP) processing, while BACE-1 (β-secretase) participates in the amyloidogenic pathway. While the former generates innocuous peptides, the latter gives rise to the toxic β-amyloid peptides believed to be responsible for Alzheimer's disease (11). In several instances, shedding at the membrane surface is followed by a "regulated intramembrane proteolysis" step within the membrane (1). This is the case for the processing of Notch ligand Delta1 and of APP, both carried out by γ-secretase after action of an α/β-secretase (11), and for signal-peptide peptidase, which removes remnants of the secretory protein translocation from the endoplasmic membrane (13).

Recently, human meprin β (Mβ) was found to specifically process APP *in vivo*, which may contribute to Alzheimer's disease (14, 15). It was also reported to activate cell-anchored α-secretase ADAM-10 and to be widely expressed in brain, intestine, kidney and skin (14, 16-18). Disruption of Mβ in mice affects embryonic viability, birth weight, and renal gene expression profiles (19). The enzyme was further identified as a sheddase or proteolytic regulator at the plasma membrane of interleukin-1β (20), interleukin-18 (21), tumor growth factor α (22), pro-collagen III (23), epithelial sodium channel (24), E-cadherin (25), tenascin-C (26), and vascular endothelial growth factor A (27). Further substrates include fibroblast growth factor 19 and connective tissue growth factor. Altered expression and activity of the enzyme is associated with pathological conditions such as inflammatory bowel disease (28), tumor progression (29), nephritis (30) and fibrosis (23).

Mβ is a 679-residue secreted multi-domain type-I membrane MP that belongs to the astacin family within the metzincins (7, 9, 16, 31, 32). The enzyme is glycosylated and assembles into either disulfide-linked homodimers or heterodimers with the closely-related meprin α subunit (33). Mβ homodimers are essentially membrane-bound but may also be shed from the surface by ADAM-10 and -17 (34, 35). To assess function, working mechanism and activation of Mβ, we analyzed the structure of the major ectoprotein of mature Mβ (MβΔC) and of its zymogen, pro-meprin β (pMβΔC). With regard to transmembrane sheddases, to date only the structures of the isolated monomeric catalytic domains of ADAM-17 (Protein Data Bank [PDB] access code 1BKC), ADAM-33 (PDB 1R55), MT1-MMP (PDB 1BUV), MT3-MMP (PDB 1RM8), BACE-1 (PDB 1FKN) and BACE-2 (PDB 2EWY) have been described. Accordingly, this is the first structural report of a multi-domain oligomeric transmembrane sheddase. This has allowed us a better understanding of the structural basis for latency and activation of this MP and to derive a plausible working mechanism for shedding of glycosylated type-I membrane substrates such as APP at the extracellular membrane surface.

RESULTS AND DISCUSSION

Multi-domain structure of pro-meprin β – We solved the crystal structures of pMβΔC (with two molecules in the asymmetric unit) and MβΔC (with one molecule; see *Supp. Information* and Supp.Table S1). The pMβΔC monomer has overall dimensions of 80×60×70Å (Fig. 1a-c) and a four-domain architecture (Supp.Fig. S2a, b) spanning an N-terminal propeptide (PD; T^{23}/E^{25}-R^{61}; Mβ residue numbering as superindices according to UniProt Q16820), a catalytic MP domain (CD; N^{62}-L^{259}), a MAM domain (S^{260}-C^{427}), and a C-terminal TRAF domain (P^{428}-S^{593}/Q^{597}). The polypeptide starts on the front surface of TRAF (Fig. 1a, c) with the first PD residues facing bulk solvent. From E^{25} to D^{30}, which includes a conserved segment among meprins ($F^{27}DVD^{30}$), the polypeptide progresses right-to-left along the TRAF surface in a nearly extended conformation and includes strand β1 (Fig. 1c; see Supp.Fig. 1a, b for nomenclature and extent of regular secondary structure elements), which is engaged in a parallel β-ribbon interaction with TRAF strand β29. In addition, F^{27} leans towards a hydrophobic pocket generated by Y^{557}, F^{532}, and M^{524} of TRAF; D^{28} interacts with S^{560}; V^{29} with Y^{557} and R^{516}; and D^{30} with both R^{516} and R^{146}, the latter from CD. TRAF residues Y^{476}, H^{478}, and A^{561} further contribute to binding. This interaction of the N-terminal segment of PD with TRAF, which buries ~460Å^2, reveals a novel potential exosite on the TRAF surface that would affect genuine substrates at sub-sites P_7'-P_{10}' when bound at the active-site cleft in reverse orientation to PD (see next and penultimate chapters). Indeed, these positions are conserved among physiological substrates (36). An example is APP, which is cleaved by Mβ at the β-secretase site (M_{671}-D_{672}; APP residue numbers as subindices according to UniProt P05067) *in vivo* and *in vitro* to generate amyloidogenic Aβ42 and Aβ41 peptides (14, 15). This entails that upon Michaelis-complex formation, APP segment D_{672}AEFRH**DS**G**Y**E_{682} occupies substrate positions P_1'-P_{11}'. The tyrosine in P_{10}' would spatially overlap with PD residue F^{27}; serine in P_8' with V^{29}; and aspartate in P_7' with D^{30}. Generally, exosites distal from the cleavage site contribute to efficient cleavage and have been previously reported for other peptidases such as thrombin (37) and ADAM family members (38).

Zymogenic determinants in pro-meprin β – At V^{29} of PD, the chain sharply kinks downwards and runs vertically until G^{32} (Fig. 1c). Here, the chain turns again and progresses horizontally at G^{32}-D^{36} to approach CD. From there on, the protein folds across the front surface of CD in reverse orientation to a substrate, thus blocking the cleft. This segment includes a helix (α1) perpendicular to the cleft. Altogether, the interaction of PD with CD buries an interface of ~1,225Å^2 and includes three salt bridges on the prime-side of the cleft (D^{30}- R^{146} and D^{34}-R^{146}) and two more on the non-prime-side (R^{54}-E^{137} and D^{56}-R^{131}). A loop in the central part of the segment enables D^{52} to chelate in a bidentate manner the catalytic zinc ion from above (Supp.Fig. S1c). In the zymogen, this residue replaces the catalytic solvent molecule of mature astacins following an "aspartate-switch" mechanism (39). At R^{57}, the chain turns down and reaches the final maturation point of pMβ, R^{61}-N^{62}. The first residue of CD is buried in the zymogen in an internal cavity framed by F^{49} and I^{53} of PD, and W^{161} and Y^{191} of CD, and its side chain interacts with E^{50} and S^{165}. Overall, the fold of PD is reminiscent of that of the propeptide of astacin except that in the latter the N-terminus is anchored to the catalytic moiety (in the absence of further domains) and helix α1 is rotated by ~70° around a vertical axis so that it rather parallels the active-site cleft (PDB 3LQ0; (39)). This means that the PDs of the two structures are only

superposable at F^{49}EGDIKLD^{56} (F^{18P}EGDIKLR^{25P} in pro-astacin; see (39)), which includes the zinc-binding aspartate. This is consistent with sequence similarity among PDs of general astacin family members being restricted to a short consensus sequence, FXGD (X stands for any residue; (32)). The short PD of Mβ and other astacins contrasts with the large pro-segments found in ADAMs, which actually constitute separate domains capable of inhibiting the CDs *in trans* (40).

The catalytic domain in pro-meprin β – The 198-residue CD is a compact ellipsoid reminiscent of a pac-man (Supp.Fig. S1a, b). A deep and narrow active-site cleft, which harbors the catalytic zinc ion at mid-width (Supp.Fig. 1c), separates an upper N-terminal and a lower C-terminal sub-domain (NTS and CTS, respectively) of similar size when viewed in standard orientation (Supp.Fig. S1a; (41)). CD is cross-linked by two disulfide bonds within the NTS: C^{103}-C^{255} connects the C-terminus of the domain with a loop, which links helix α2 and strand β3 (Lα2β3) and C^{124}-C^{144} connects β5 with Lβ6α3 and contributes thus to shaping the upper-rim of the active-site cleft on its prime side. NTS harbors a central twisted five-stranded β-sheet (β2-β6) whose lowermost and only antiparallel strand (β5) shapes the upper-rim of the active-site cleft. The sheet is decorated on its concave bottom by two helices, the "backing helix" (α2) and the "active-site helix" (α3), which run nearly parallel to the strands of the sheet. Helix α3 includes the first part of a long zinc-binding consensus sequence, H^{152}EXXHXXGXXH^{162} (Supp.Fig. S1c), which is found in astacins but also metzincins in general (7-9, 42, 43). This helix ends at G^{159}, which allows for a sharp turn of the polypeptide chain in order to enter CTS. The latter contains the third zinc-binding residue, H^{162}, and the "family-specific" residue of astacins, E^{163} (43, 44). Also typical for astacins and metzincins, a tight 1,4-β-type "Met-turn" is located below the catalytic zinc-site featuring a strictly conserved methionine, M^{209} (Supp.Fig. S1c)(8, 45). The rest of CTS has little regular secondary structure further to the major "C-terminal helix" (α4; Supp.Fig. S1a, b). Of particular interest is that the polypeptide chain is disordered at Y^{191}/D^{194}-S^{198}/L^{199}. This segment corresponds to the "activation domain" in astacins (39).

The MAM and TRAF domains in pro-meprin β – After CD, the polypeptide chain enters the 168-residue MAM domain, which lies behind TRAF and performs no contact with the MP moiety with the exception of some residues near the inter-domain junction (Fig. 1a, right). MAM is a β-sandwich consisting of two five-stranded antiparallel β-sheets rotated away from each other by ~25º. The sandwich consists of a front sheet twisted by ~70º (β10-β13-β18-β15-β16; see Supp.Fig. S1a, b, center) and a back sheet twisted by ~40º and curled (β11-β9+β12-β19-β14-β17), whose second strand (β9+β12) is interrupted by 3_{10}-helix η3 and strands β10 and β11. Overall, the β-sandwich is built following a "jelly-roll" architecture made up of two four-stranded Greek-key motifs (Supp.Fig. S1b, center, in red and magenta, respectively), in which the second motif is inserted after the first β-ribbon (β9+β12-β13) of the first motif. The jelly roll is decorated by the aforementioned insertion (Supp.Fig. S1b, center, in pink), which includes Lβ10β11–partially undefined in one of the two molecules in the asymmetric unit–and Lβ11β12, the "dimerization loop" (see below). In addition, the pairs C^{265}-C^{273} and C^{340}-C^{427} are at adequate distance and geometry for disulfide bonding but, contrary to the SS-bonds in CD, the respective Sγ atoms are 2.9Å apart. We attribute this to a radiation-damage artifact due to the long exposure time required to collect a complete dataset in space group P1. In addition, the η3-β10-β11 insertion contributes to an octahedral cation-binding site tentatively interpreted as a sodium

site. The ion is coordinated by the side chains of E^{268}, D^{298}, S^{300}, D^{418}, and the main-chain oxygen atoms of S^{266} and F^{310} (Supp.Fig. S1d). Overall, the topology and architecture of this domain is reminiscent of receptor-type tyrosine-protein phosphatase μ (PDB 2V5Y), which belongs to the MAM protein family of adhesive proteins initially identified by bioinformatic searches in meprin α and β, A5 protein, and receptor protein tyrosine phosphatase μ (46). In particular, the MAM domain of tyrosine phosphatase μ was shown to play a major role in homodimerization of the phosphatase ectoprotein and in cell adhesion (47).

Downstream of MAM, the 170-residue TRAF domain interacts with the former burying an interface of ~650Å^2 (Fig. 1a, right). TRAF also interacts with CD through a surface spanning ~950Å^2 in one protomer and ~1170Å^2 in the other as the polypeptide chain could be traced for four residues more in the latter. TRAF features the second type of all-β structure found in pMβ (Supp.Fig. S1a,b, right), with a five-stranded front sheet (β21-β22-β23-β29-β28) and a four-stranded back antiparallel sheet (β20-β30-β24-β25) rotated by ~40º against each other and arranged in a β-sandwich as in MAM. The front sheet is twisted by ~50º, arched and curled, while the back sheet is just twisted by ~50º. Altogether, the strands are arranged as two Greek-key motifs (Supp.Fig. S1b, right, in purple and violet), in which the second one is inserted between strands #3 (β30) and #4 (β23) of the first one instead of after the first β-ribbon as in MAM (see above). Again contrary to MAM, which features a jelly roll with parallel Greek keys, in TRAF the second Greek key is rotated by ~180º relative to the first one around an axis perpendicular to the plane of the β-sheets. In TRAF, the double Greek key is decorated with a β-ribbon (β26-β27) after β25, an additional short strand (β28) for the front sheet, and a helix (α5) between β29 and β30 (all in blue in Supp.Fig. S1b, right). The only cysteine found in this domain, C^{492}, is buried and unbound, and the C-terminus of the molecule (S^{593}/Q^{597}) protrudes from the top surface of the monomer (Fig. 1a, left). Overall, Mβ TRAF is structurally similar to tumor-necrosis factor receptor-associated factors 2, 3, and 6 (e.g. PDB 1LB5). These gave rise to the TRAF family, which comprises major mediators of cell activation engaged in homo- and hetero-dimerization (48).

Glycosylation sites and "sugar channel" **–** The pMβΔC and MβΔC structures contained sugar moieties attached to residues N^{218} and N^{254} of CTS; N^{370} of MAM; and N^{436}, N^{445}, N^{547}, and N^{592} of TRAF. The observed *N*-glycosylation patterns, which are consistent with those found in other recombinant proteins produced in *Trichoplusia ni* insect cells (49), are similar to those found in mammalian glycosylation pathways (50) (see Supp.Fig. S2). Accordingly, it is assumed that the glycosylations, which were able to be modeled to up to ten hexose moieties at a single site (N^{547}) and a maximum of 26 hexoses per protein monomer (see Supp.Fig. S1b for details), represent a bona fide mimic of the authentic glycosylation pattern of the enzyme. While the sugar moieties attached to N^{218} and N^{254} point to the bulk solvent and are isolated in the monomer structure, those of the remaining five sites are all oriented toward the inter-domain space between MAM and TRAF, although they do not contact each other (Fig. 1a, right). Given this accumulation, we termed the lumen between MAM and TRAF "sugar channel".

Dimerization of pro-meprin β **–** Two pMβΔC monomers associate to form a compact ellipsoid with dimensions of 115×65×90Å burying an interface of ~1,220Å^2 (4.5% of the total monomer surface; Fig. 1d, e). Superposition of the whole monomers (*rmsd* of 0.84Å for 548 common Cα atoms) reveals that while PDs, NTSs, and TRAFs perfectly fit together, slight deviations are observed for CTSs and MAMs, which lead to displacements of up to

2.8Å (measured at S^{182} Cα) and 2.6Å (at A^{410} Cα), respectively. Dimerization occurs through nearly symmetric interactions between CD of one monomer and MAM of the other. Segments involved include the beginning of β2, 3_{10}-helix η1, Lη2β8, the sugar moiety attached to N^{254}, and the C-terminal tail of CD; and Lβ9η3, η3, Lη3β10, β13, Lβ13β14, and β18 of MAM. This is consistent with the general oligomerization and protein-protein interaction function of MAM domains (see above). Notably, the dimerization loop of both polypeptide chains point into the center of the particle. They are disordered at segment M^{302}-Q^{306}/G^{307}, which includes residue C^{305}. This residue is engaged in an inter-molecular disulfide bond cross-linking the dimer as shown by non-reducing SDS-PAGE of carefully washed and dissolved crystals, thus suggesting a function as a double safeguard rather than a feature indispensable for dimerization. In the particle, the glycans attached at N^{254} of each monomer interact with each other and contribute thus to a small hydrophilic cluster on the surface (see below). Moreover, the two CDs (with their attached PDs), as well as the sugar channels, are accessible at opposite ends of the particle, which is consistent with a competent conformation for substrate binding (Fig. 1d, right), and both C-termini of the dimer are located on the same face of the particle (Fig. 1d,e). Given that the complete ectoprotein only comprises a further ~60 residues, which mainly contribute to a compact EGF domain (C^{608}-C^{643}) before the transmembrane anchor (I^{653}-V^{673}), this face is likely to be membrane-proximal and this allowed us to orient the particle with respect to the extracellular plasma membrane surface (Fig. 1d, left). Further evidence for the consistency of this orientation is based on the proximity of the CDs and their active-site clefts to the membrane surface, which is required if membrane-anchored substrates are to be cleaved close to the membrane.

Activation to mature meprin β – Activation of meprins requires proteolysis of the N-terminal PD, which is catalyzed by trypsin in the intestinal lumen and kallikrein-related peptidases (KLK-4, -5 and -8) in other tissues (17, 51). Comparison of the zymogenic and mature structures, which were obtained in different crystal forms, reveals that in general the dimers (established in MβΔC between symmetry equivalents) fit together with a global *rmsd* of 1.2Å for 1,006 common Cα atoms (out of 561+554 residues in pMβΔC and 533+533 in MβΔC; Supp.Fig. S3a). Detailed inspection, however, shows that CTSs undergo major rearrangement upon maturation through a hinge rotation of ~25º towards the cleft around E^{163}, H^{210}, and G^{236}, which entails a maximum displacement of ~8Å (at G^{183} Cα; see Supp.Fig. S3b-d). In this way, the space exposed by PD removal is subsequently occupied in part by CTS. This closing hinge motion further causes displacement of the mature N-terminus of Mβ and a rotation of its first three residues by ~180º. Thus, N^{62} becomes completely buried inside the mature CD moiety and hydrogen-bonded through its Nδ2 atom to the side chain of the family-specific residue E^{163}. The latter has the same side-chain conformation as in the zymogen and is likewise bound to K^{248} through a buried salt bridge. Maturation further entails rigidification of the formerly flexible activation segment (see above) and its upwards shift towards the cleft by ~4Å (at Y^{191} Cα). This leads to a competent conformation that enables D^{197}O and S^{196}Oγ to bind the α-amino group of N^{62} (Supp.Fig. S3c,d). The stiffening of CD contributes to the traceability of MβΔC structure along its entire polypeptide chain (N^{62}-T^{594}). This holds true also for the flexible loop Lβ11β12, which encompasses the inter-molecular disulfide bond, although this is based on weak electron density. A further key role in CTS rearrangement is played by W^{161}, whose side chain rotates by ~180º around its χ_2 angle and becomes sandwiched by the ascending side chain of Y^{191} of the activation segment. Overall, the major rearrangement observed is compatible with the gross particle structure, indicating that the zymogen is already in a

preformed conformation adequate for catalysis, which requires only a rigid-body rearrangement of a sub-domain spanning 1/7 of the full-length protein for full competence.

Maturation also constricts the active-site cleft and this affects the side chain of Y^{211}, which is engaged in zinc and substrate binding, and catalysis in mature astacin CDs (i.e. the "tyrosine-switch" residue; (52)) and some other metzincins such as serralysins and pappalysins (8). In the zymogen, it is pulled away from its competent position by the intercalation of PD helix α1, in particular the side chains of I^{37}-F^{38} (Fig. 1b), and removal of PD allows Y^{211} to approach the catalytic ion (replaced in the MβΔC structure with a cadmium; see *Supp. Information*). There is additional electron density on the prime-side of the active-site cleft of the mature enzyme–potentially corresponding to a substrate or inhibitor with low occupancy, which was conservatively interpreted as a glycerol molecule. Most noteworthy, R^{238}, engaged in a salt bridge with D^{36} in the zymogen (see above), becomes reoriented with regard to its side chain and occupies the space of D^{36}-I^{37} of PD. This arginine is found within a segment mainly engaged in shaping the S_1' pocket in astacins, the "170-loop" (32), and in Mβ it accounts for its preference for acidic residues in this sub-site (see Supp.Fig. S3 and (36)). Further inspection of the active-site cleft and the adjacent exosite provided by TRAF (see first chapter) reveals that R^{146} and R^{516} (to the right of R^{238} in Fig. 1b,c), and R^{184} from Lβ7η2 of CD, which interacts with E^{42} in the zymogen and becomes reoriented upon maturation (Supp.Fig. S3b-d), could explain the preference of Mβ for acidic side chains also in downstream prime-side sub-sites (see first chapter), pinpointing a unique cleavage specificity among extracellular proteases (36).

Finally, the substrate specificity of Mβ is complementary to that of other physiologically relevant transmembrane sheddases. The most studied ones, ADAM-17, ADAM-10, and MT1-MMP, as well as other ADAM and MMP family members, have specificity for large and medium-sized hydrophobic residues in P_1' as found, for example, in ADAM-17 substrates (53) and the α-secretase site of APP (K_{687}-L_{688}). BACE-2 also cleaves at the α-secretase site (54). Accordingly, Mβ would be the only transmembrane sheddase capable of cleaving before acidic residues in general and at the β-secretase site of APP in particular in addition to BACE-1 (15).

A working mechanism for shedding at the plasma membrane – The structures of both pMβΔC and MβΔC reveal a dimer with a membrane-proximal face (see above). We constructed a homology model for the remaining ~60 residues of the ectoprotein–mainly encompassing an EGF-like domain–, the 20-residue transmembrane anchor, and the 27-residue cytosolic tail of each monomer (see *Supp. Information*), which enabled us to propose a molecular mechanism for Mβ-mediated shedding at the plasma membrane (Fig. 2). This is visualized utilizing a tentative model for APP region F_{624}-L_{723}, which includes the final segment of the ectoprotein and the transmembrane helix (55) and, thus, the β-secretase cleavage site (see first chapter). Following this model, a substrate chain would be bound at the membrane-distal part (F_{624}-V_{640} of APP) by the sugar channel of Mβ monomer one, whose two major glycosylations at N^{547} of MAM and N^{370} of TRAF would act like a bat-winged saloon door to admit and retain the substrate chain. This would be consistent with the general function of such domains in protein-protein interactions. Downstream, the substrate chain would run along the back surface of the cognate CD until position L_{650} to approach the interface between CDs within the dimer and, eventually, enter the active-site cleft of Mβ monomer two (Fig. 2). An intra-

molecular mechanism involving all three domains of one monomer is unlikely as the substrate would have to undergo a long excursion after passing through the sugar channel and the back surface of the cognate CD to reach its active-site cleft with the correct N-to-C polarization (Fig. 1e). The first residue after the β-secretase cleavage site, D_{672}, would be located in the S_1' pocket of Mβ, thus matching its substrate specificity. Further downstream sub-sites of the substrate would run across the cleft and the prime-site exosite on the TRAF surface (see first chapter) of Mβ monomer two and then turn down to reach the APP transmembrane segment at G_{700}. Generally, the substrate would follow an "N-like" trajectory (Fig. 2 top right) and involve domains from both monomers within the Mβ-dimer. In addition, this mechanism would be sugar-assisted. The majority of potential shedding substrates (87% of single-pass transmembrane proteins; (56)) are glycosylated, and this holds true also for APP and other Mβ substrates. In particular, APP is glycosylated at T_{633}, T_{651}, T_{652}, T_{659}, T_{663}, S_{667}, and Y_{681} with regard to the segment under inspection here (57). Of these sites, the proposed model predicts that the latter three could be at or close to sub-sites P_5, P_7, and P_{10}', i.e. they would not interact with the enzyme but rather solvent exposed. By contrast, the glycans attached to T_{651}, T_{652}, and T_{659} could potentially interact with the site created by the symmetric N^{254} glycosylations of Mβ, and the one at T_{633} with that of Mβ N^{436} (Fig. 2). Overall, this mechanism would be compatible with other type-I transmembrane substrates that are shed at sites at least 20-25 residues above the membrane. The different *N*-glycans found on the surface of the Mβ particle along the proposed substrate path (see Fig. 2) could provide alternative anchor points for the particular sugar moieties of each substrate.

MATERIALS AND METHODS

A detailed description of procedures is provided under *Supp*. *Information*. Briefly, pMβΔC was produced by recombinant baculovirus-induced overexpression in insect cells and activated by trypsin as reported (58). The structure of pMβΔC was solved by a combination of single-wavelength anomalous diffraction and Patterson search. The structure of MβΔC was solved by Patterson search. A model for full-length Mβ was obtained by connecting a homology model for the EGF-like domain with the experimental structure and a modeled transmembrane helix *plus* cytosolic tail by linkers of stereochemically reasonable conformation.

REFERENCES

1. Blobel CP (2005) ADAMs: key components in EGFR signalling and development. *Nat Rev Mol Cell Biol* 6:32-43.
2. Arribas J, Merlos-Suárez A (2003) Shedding of plasma membrane proteins. *Curr Top Dev Biol* 54:125-144.
3. Pandiella A, Bosenberg MW, Huang EJ, Besmer P, Massague J (1992) Cleavage of membrane-anchored growth factors involves distinct protease activities regulated through common mechanisms. *J Biol Chem* 267:24028-24033.
4. Edwards DR, Handsley MM, Pennington CJ (2008) The ADAM metalloproteinases. *Mol Aspects Med* 29:258-289.
5. Saftig P, Reiss K (2011) The "A Disintegrin And Metalloproteases" ADAM10 and ADAM17: novel drug targets with therapeutic potential? *Eur J Cell Biol* 90:527-535.
6. Murphy G, Nagase H (2011) Localizing matrix metalloproteinase activities in the pericellular environment. *FEBS J* 278:2-15.
7. Gomis-Rüth FX (2003) Structural aspects of the *metzincin* clan of metalloendopeptidases. *Mol Biotech* 24:157-202.
8. Gomis-Rüth FX (2009) Catalytic domain architecture of metzincin metalloproteases. *J Biol Chem* 284:15353-15357.
9. Stöcker W et al. (1995) The metzincins - Topological and sequential relations between the astacins, adamalysins, serralysins, and matrixins (collagenases) define a superfamily of zinc-peptidases *Prot Sci* 4:823-840.
10. Barbolina MV, Stack MS (2008) Membrane type 1-matrix metalloproteinase: substrate diversity in pericellular proteolysis. *Semin Cell Dev Biol* 19:24-33.
11. Dislich B, Lichtenthaler SF (2012) The membrane-bound aspartyl protease BACE1: molecular and functional properties in Alzheimer's disease and beyond. *Front Physiol* 3:1-16.
12. Olivieri A et al. (2011) Juxtamembrane shedding of *Plasmodium falciparum* AMA1 is sequence independent and essential, and helps evade invasion-inhibitory antibodies. *PLoS Pathog* 7:e1002448.
13. Weihofen A, Binns K, Lemberg MK, Ashman K, Martoglio B (2002) Identification of signal peptide peptidase, a presenilin-type aspartic protease. *Science* 296:2215-2218.
14. Jefferson T et al. (2011) Metalloprotease meprin β generates nontoxic N-terminal amyloid precursor protein fragments *in vivo*. *J Biol Chem* 286:27741-27750.
15. Bien J et al. (2012) The metalloprotease meprin β generates amino terminal truncated Aβ-peptide species. *J Biol Chem* in press.
16. Sterchi EE, Stöcker W, Bond JS (2008) Meprins, membrane-bound and secreted astacin metalloproteinases. *Mol Aspects Med* 29:309-328.
17. Becker-Pauly C et al. (2007) The α and β subunits of the metalloprotease meprin are expressed in separate layers of human epidermis, revealing different functions in keratinocyte proliferation and differentiation. *J Invest Dermatol* 127:1115-1125.
18. Schütte A, Lottaz D, Sterchi EE, Stöcker W, Becker-Pauly C (2007) Two α subunits and one β subunit of meprin zinc-endopeptidases are differentially expressed in the zebrafish *Danio rerio*. *Biol Chem* 388:523-531.
19. Norman LP, Jiang W, Han X, Saunders TL, Bond JS (2003) Targeted disruption of the meprin β gene in mice leads to underrepresentation of knockout mice and changes in renal gene expression profiles. *Mol Cell Biol* 23:1221-1230.
20. Herzog C et al. (2009) Meprin A and meprin alpha generate biologically functional IL-1beta from pro-IL-1beta *Biochem Biophys Res Commun* 379:904-908.
21. Banerjee S, Bond JS (2008) Prointerleukin-18 is activated by meprin β *in vitro* and *in vivo* in intestinal inflammation. *J Biol Chem* 283:31371-31377.
22. Bergin DA et al. (2008) Activation of the epidermal growth factor receptor (EGFR) by a novel metalloprotease pathway. *J Biol Chem* 283:31736-31744.
23. Kronenberg D et al. (2010) Processing of procollagen III by meprins: new players in extracellular matrix assembly? *J Invest Dermatol* 130:2727-2735.
24. Bondarava M, Li T, Endl E, Wehner F (2009) α-ENaC is a functional element of the hypertonicity-induced cation channel in HepG2 cells and it mediates proliferation. *Pflügers Arch* 458:675-687.

25. Huguenin M et al. (2008) The metalloprotease meprinbeta processes E-cadherin and weakens intercellular adhesion. *PLoS One* 3:e2153.
26. Ambort D et al. (2010) Specific processing of tenascin-C by the metalloprotease meprin β neutralizes its inhibition of cell spreading. *Matrix Biol* 29:31-42.
27. Schütte A, Hedrich J, Stöcker W, Becker-Pauly C (2010) Let it flow: Morpholino knockdown in zebrafish embryos reveals a pro-angiogenic effect of the metalloprotease meprin α2. *PLoS One* 5:e8835.
28. Vazeille E et al. (2011) Role of meprins to protect ileal mucosa of Crohn's disease patients from colonization by adherent-invasive *E. coli*. *PLoS One* 6:e21199.
29. Lottaz D et al. (2011) Enhanced activity of meprin-α, a pro-migratory and pro-angiogenic protease, in colorectal cancer. *PLoS One* 6:e26450.
30. Oneda B et al. (2008) Metalloprotease meprin β in rat kidney: glomerular localization and differential expression in glomerulonephritis. *PLoS One* 3:e2278.
31. Bond JS, Beynon RJ (1995) The astacin family of metalloendopeptidases. *Prot Sci* 4:1247-1261.
32. Gomis-Rüth FX, Trillo-Muyo S, Stöcker W (2012) Functional and structural insights into astacin metallopeptidases. *Biol Chem* 393:in press.
33. Bertenshaw GP, Norcum MT, Bond JS (2003) Structure of homo- and hetero-oligomeric meprin metalloproteases. Dimers, tetramers, and high molecular mass multimers. *J Biol Chem* 278:2522-2532.
34. Hahn D et al. (2003) Phorbol 12-myristate 13-acetate-induced ectodomain shedding and phosphorylation of the human meprinβ metalloprotease. *J Biol Chem* 278:42829-42839.
35. Jefferson T et al. (2012) The substrate degradome of meprin metalloproteases reveals an unexpected proteolytic link between meprin β and ADAM10. *Cell Mol Life Sci* 29:in press.
36. Becker-Pauly C et al. (2011) Proteomic analyses reveal an acidic prime side specificity for the astacin metalloprotease family reflected by physiological substrates. *Mol Cell Proteomics* 10:M111 009233.
37. Bode W, Turk D, Karshikov A (1992) The refined 1.9-Å X-ray crystal structure of D-Phe-Pro-Arg chloromethylketone-inhibited human α-thrombin: structure analysis, overall structure, electrostatic properties, detailed active-site geometry, and structure-function relationships. *Protein Sci* 1:426-471.
38. Gao W et al. (2012) Rearranging exosites in non-catalytic domains can redirect the substrate specificity of ADAMTS proteases *J Biol Chem* 287:in press.
39. Guevara T et al. (2010) Proenzyme structure and activation of astacin metallopeptidase. *J Biol Chem* 285:13958-13965.
40. Moss ML et al. (2007) The ADAM10 prodomain is a specific inhibitor of ADAM10 proteolytic activity and inhibits cellular shedding events. *J Biol Chem* 282:35712-35721.
41. Gomis-Rüth FX, Botelho TO, Bode W (2012) A standard orientation for metallopeptidases. *Biochim Biophys Acta* 1824:157-163.
42. Bode W, Gomis-Rüth FX, Stöcker W (1993) Astacins, serralysins, snake venom and matrix metalloproteinases exhibit identical zinc-binding environments (HEXXHXXGXXH and Met-turn) and topologies and should be grouped into a common family, the ´metzincins´. *FEBS Lett* 331:134-140.
43. Stöcker W, Gomis-Rüth FX, Bode W, Zwilling R (1993) Implications of the three-dimensional structure of astacin for the structure and function of the astacin-family of zinc-endopeptidases *Eur J Biochem* 214:215-231.
44. Bode W, Gomis-Rüth FX, Huber R, Zwilling R, Stöcker W (1992) Structure of astacin and implications for activation of astacins and zinc-ligation of collagenases. *Nature* 358:164-167.
45. Goulas T, Arolas JL, Gomis-Rüth FX (2010) Structure, function and latency regulation of a bacterial enterotoxin potentially derived from a mammalian adamalysin/ADAM xenolog. *Proc Natl Acad Sci USA* 108:1856-1861.
46. Beckmann G, Bork P (1993) An adhesive domain detected in functionally diverse receptors *Trends Biochem Sci* 18:40-41.
47. Aricescu AR et al. (2007) Structure of a tyrosine phosphatase adhesive interaction reveals a spacer-clamp mechanism. *Science* 317:1217-1220.
48. Zapata JM et al. (2001) A diverse family of proteins containing tumor necrosis factor receptor-associated factor domains *J Biol Chem* 276:24242-24252.
49. Ailor E et al. (2000) *N*-glycan patterns of human transferrin produced in *Trichoplusia ni* insect cells: effects of mammalian galactosyltransferase. *Glycobiology* 10:837-847.

50. Harrison RL, Jarvis DL (2006) Protein *N*-glycosylation in the baculovirus-insect cell expression system and engineering of insect cells to produce "mammalianized" recombinant glycoproteins. *Adv Virus Res* 68:159-191.
51. Ohler A, Debela M, Wagner S, Magdolen V, Becker-Pauly C (2010) Analyzing the protease web in skin: meprin metalloproteases are activated specifically by KLK4, 5 and 8 *vice versa* leading to processing of proKLK7 thereby triggering its activation. *Biol Chem* 391:455-460.
52. Grams F et al. (1996) Structure of astacin with a transition-state analogue inhibitor *Nature Struc Biol* 3:671-675.
53. Maskos K et al. (1998) Crystal structure of the catalytic domain of human tumor necrosis factor-α-converting enzyme. *Proc Natl Acad Sci U S A* 95:3408-3412.
54. Thinakaran G, Koo EH (2008) Amyloid precursor protein trafficking, processing, and function. *J Biol Chem* 283:29615-29619.
55. Barrett PJ et al. (2012) The amyloid precursor protein has a flexible transmembrane domain and binds cholesterol. *Science* 336:1168-1171.
56. Kuhn P-H et al. (2012) Secretome protein enrichment identifies physiological BACE1 protease substrates in neurons. *EMBO J* 31:in press.
57. Halim A et al. (2011) Site-specific characterization of threonine, serine, and tyrosine glycosylations of amyloid precursor protein/amyloid beta-peptides in human cerebrospinal fluid. *Proc Natl Acad Sci USA* 108:11848-11853.
58. Becker C et al. (2003) Differences in the activation mechanism between the alpha and beta subunits of human meprin. *Biol Chem* 384:825-831.

FIGURE LEGENDS

Figure 1 – Structure of pro-meprin β. (A) The structure of the pMβΔC monomer shown in front (left panel; CD in standard orientation according to (41)) and top (right panel) reference views. The latter is along the sugar channel (green arrow). Glycans are depicted as stick models and the respective asparagine residues are numbered. The corresponding surface models are depicted above each picture (glycans in white). PD is shown in ochre, CD in aquamarine, MAM in red, and TRAF in purple. The zinc and the sodium ions are shown as magenta and blue spheres, respectively. **(B)** Close-up view in stereo of (A), left panel, to highlight residues engaged in PD-CD interactions. **(C)** Same as (B) in mono for the interaction between PD and TRAF. The first two residues of the structure (P^{23}-W^{24}) are actually T^{23}-P^{24} in the natural protein (see *Supp. Information*). **(D)** pMβΔC dimer superposed with its Connolly surface shown in the front (left panel; in a plane with the membrane) and bottom (right panel) dimer reference views. PDs are shown in ochre and yellow, CDs in aquamarine and blue, MAMs in red and green, TRAFs in purple and pink, and sugar moieties in white and gray. The intermolecular twofold axis is shown in red and green arrows point at the sugar channels. **(E)** Cartoon depicting the dimer as a ribbon in front (left panel) and bottom (right panel) views as in (D). Green arrows run along the sugar channels and a pink arrow highlights the cleft of one CD with the adequate orientation of a substrate. The segment containing the inter-molecular disulfide bond between C^{305} residues is disordered in the zymogen and its approximate position is highlighted by orange ellipses.

Figure 2 – Sheddase mechanism of meprin β. Working model of Mβ function based on the experimental dimer (CDs in aquamarine and turquoise, MAMs in orange and red, TRAFs in mauve and purple, and glycosylation moieties in light green) in front (top panel) view (see Fig. 1d, left) and top (from the membrane surface; bottom panel) view from the membrane (here the membrane was removed for clarity). The segments present in the Mβ dimer but missing in the experimental MβΔC structure (EGF, transmembrane (TM), and cytosolic tail (CST)) have been computationally modeled (see *Supp. Information*) and are shown in white/light blue. A transmembrane substrate model for APP (segment 624-723) is shown as a blue ribbon. The substrate segment proposed to interact with the dimer partner is depicted in pale blue to highlight that this part of the mechanism is more speculative. APP glycosylation sites relevant for the proposed mechanism are marked in yellow on the ribbon and labeled. In the top image, red ellipses highlight sugars attached to N^{436} of the right monomer (bottom ellipse) and to N^{254} of both monomers (top ellipse). The bottom image only shows the latter ellipse. Top right insert, a possible "N-like" trajectory of the substrate.

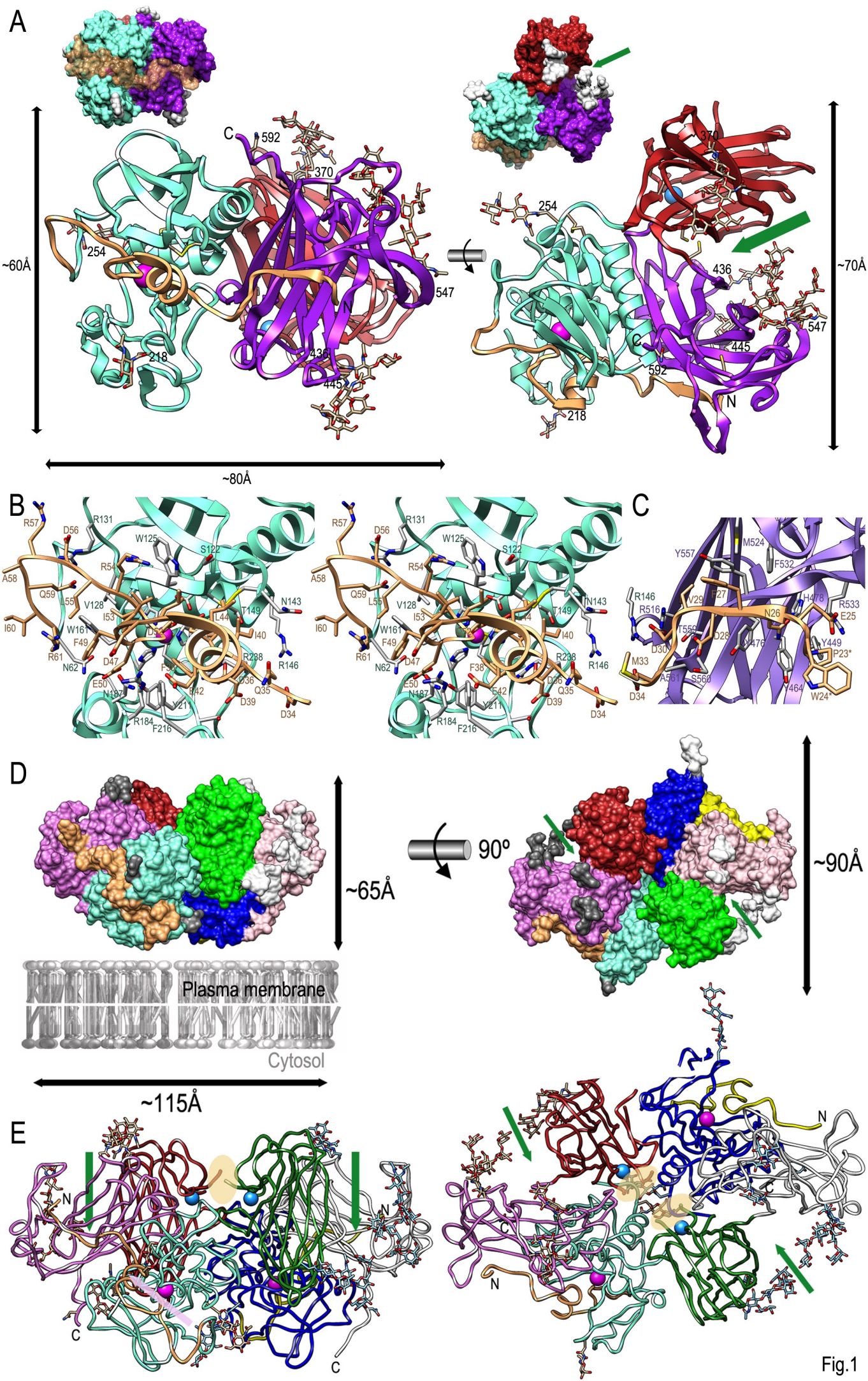
A
~60Å
~80Å
~70Å
C
592
370
254
547
N
436
218
445
B
C
D
~65Å
90°
~90Å
Plasma membrane
Cytosol
~115Å
E

Fig.1

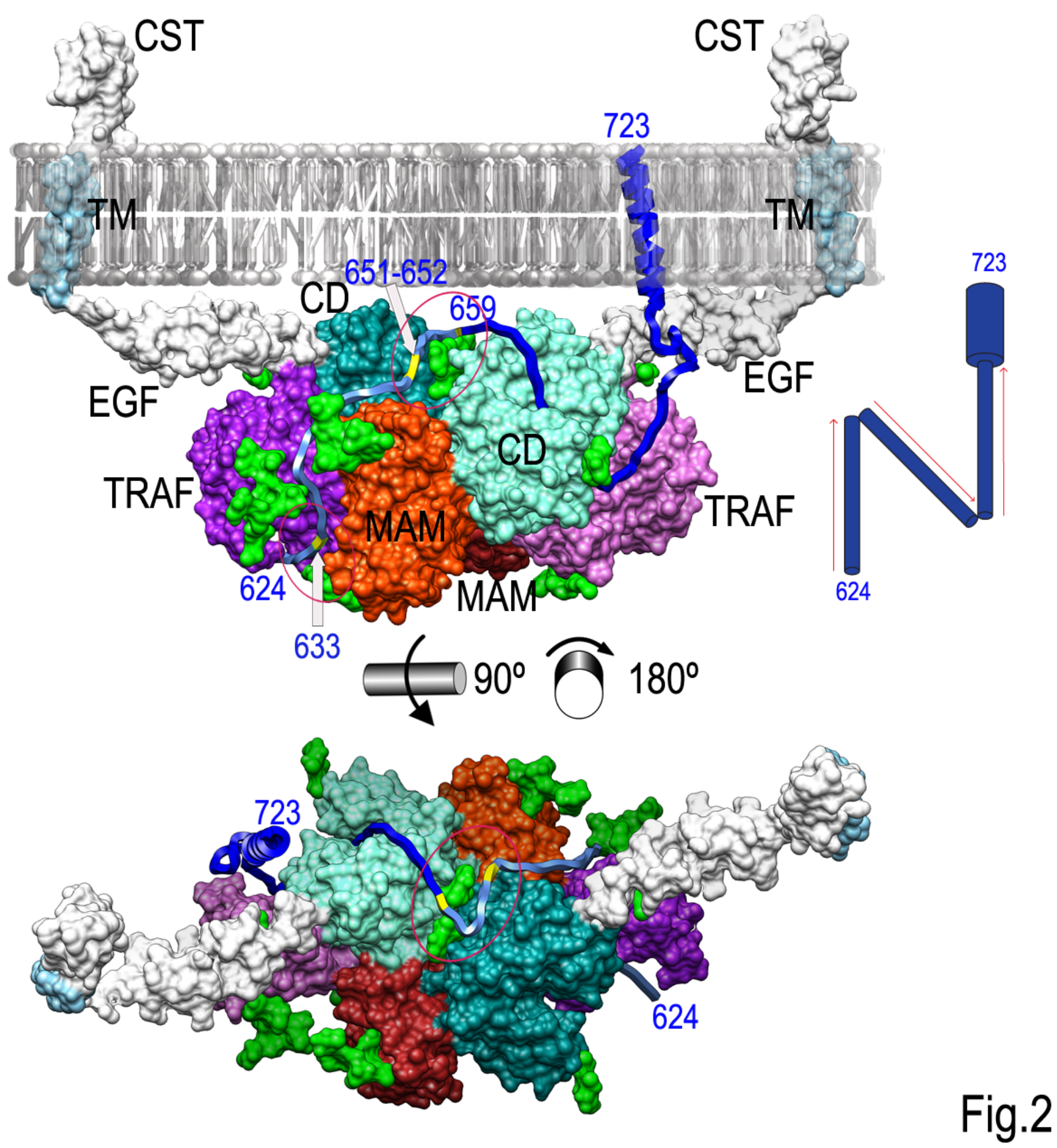
CST
CST
723
TM
TM
651-652
CD
659
EGF
EGF
CD
TRAF
TRAF
MAM
MAM
624
633
723
624
90º
180º
723
624

Fig.2

SUPPORTING INFORMATION

1. EXPERIMENTAL PROCEDURES

Protein production — The pro-meprin β ectomoiety lacking the N-terminal signal peptide and the C-terminal 87 residues (numbering according to the pre-pro-sequence, UniProt Q16820), hereafter referred to as pMβΔC, was produced by recombinant baculovirus-induced overexpression in *Trichoplusia ni* insect cells and activated by trypsin to yield mature meprin β (MβΔC) as reported (1). In the expression construct T^{23}-P^{24} were replaced with P^{23}-W^{24}.

Crystallization and structure solution — Crystallization assays were performed by the sitting-drop vapor diffusion method. Reservoir solutions were prepared by a Tecan robot and 100-nL crystallization drops were dispensed on 96x2-well MRC plates (Innovadyne) by a Phoenix nanodrop robot (Art Robbins) at the High-Throughput Crystallography Platform (PAC) of the Barcelona Science Park. Plates were stored in Bruker steady-temperature crystal farms at 4°C and 20ºC. Successful conditions were scaled up to the microliter range with 24-well Cryschem crystallization dishes (Hampton Research). pMβΔC at ~7.0mg/mL in 20mM HEPES pH7.5 was crystallized at 20ºC from equivolumetric drops with 18.2% polyethylene glycol 8,000; 1M LiCl; 0.1M bicine pH9.0 as reservoir solution. MβΔC at ~6.8mg/mL in 20mM HEPES pH7.5; 1mM phenylmethylsulfonyl fluoride; 100μM actinonin was crystallized using 20% polyethylene glycol 3,350; 0.2M sodium malonate; 0.1M bis-tris propane pH8.5 as reservoir solution, and 0.1M $CdCl_2$ as an additive. Crystals were cryo-protected by immersion in harvesting solutions (25% polyethylene glycol 3,350; 1M LiCl; 0.1M bicine pH9.0 for pMβΔC; 25% polyethylene glycol 3,350; 0.2M sodium malonate; 0.1M bis-tris propane pH8.5 for MβΔC) supplemented stepwise with glycerol (0-15% for pMβΔC; 0-20% for MβΔC). Complete diffraction datasets were collected from liquid-N_2 flash-cryo-cooled crystals at 100K (provided by an Oxford Cryosystems 700 series cryostream) on a ADSC Q315R CCD and a Pilatus 6M pixel detector at beam lines ID23-1 (pMβΔC) and ID29 (MβΔC), respectively, of the European Synchrotron Radiation Facility (ESRF, Grenoble, France) within the Block Allocation Group "BAG Barcelona." Crystals were triclinic (pMβΔC) and hexagonal (MβΔC), with two and one molecules per asymmetric unit, respectively. Diffraction data were integrated, scaled, merged, and reduced with programs XDS (2) and SCALA (3) within the CCP4 suite of programs (4) (see Supp.Table S1).

The structure of pMβΔC was solved by a combination of single-wavelength anomalous diffraction and Patterson search. The latter was performed with program PHASER (5) with the structure of crayfish pro-astacin (PDB 3LQ0; (6)), adequately trimmed and modified for its side chains with program CHAINSAW (7), as searching model for the catalytic domain and part of the pro-segment; this gave two unambiguous solutions with space group P1. Diffraction data to 2Å resolution of a crystal collected at the zinc K-edge peak wavelength, as inferred from a previous XANES fluorescence scan, enabled program SHELXD (8) to independently identify the two zinc sites of the dimer present in the asymmetric unit. Subsequent phasing with these two sites using program SHELXE and higher-resolved diffraction data to 1.85Å resolution as a pseudo-native dataset, combined with the calculated phases of the two Patterson-search solutions, yielded a suitable electron density map for chain tracing on a Silicon Graphics Octane2 Workstation using program TURBO-FRODO (9). Model building of the four domains–propeptide (PD), catalytic domain (CD), MAM

domain, and TRAF domain–of the two molecules alternated with crystallographic refinement with program BUSTER/TNT (10), which included TLS refinement and, initially, NCS restraints, until completion of the model. The final model of pMβΔC comprised residues 25-193+200-301+308-597 of molecule A and 23-190+199-277+282-301+307-593 of molecule B. Out of the ten cysteine residues of the sequence, four made two disulfide bonds in the CD (C^{103}-C^{255} and C^{124}-C^{144}); two more pairs of MAM (C^{265}-C^{273} and C^{340}-C^{427}) were at adequate distance for disulfide bonding but were unbound, probably due to a radiation-damage artifact resulting from the long exposure time required to collect a complete dataset in space group P1; C^{305} of MAM was in a flexible segment but was engaged in an inter-molecular disulfide bond as revealed by non-reducing SDS PAGE; and C^{492} of TRAF was unpaired. In addition, each protomer contained a zinc and a (tentative) sodium cation. *N*-linked glycosylations were found attached to residues 218, 254, 370, 436, 445, and 547 of each monomer. These comprised 10(10) *N*-acetylglucosamine, 8(7) α-D-mannose, 3(5) α-L-fucose, and 4(2) β-D-mannose moieties in total for monomer A (monomer B) according to the overall scheme depicted in Suppl.Fig. S2. Five tentative chloride ions, one glycerol molecule, and 808 solvent molecules completed the model.

The structure of MβΔC was solved by Patterson search with program PHASER. Each of the three domains shared with the zymogen was used as an independent searching model. Model completion and refinement with BUSTER/TNT proceeded as aforementioned except that structurally equivalent parts of the higher-resolved zymogen structure were used to restrain refinement of the low-resolution mature enzyme structure. The final model of MβΔC comprised residues 62-594 of the single crystallographically-independent molecule (monomer A) *plus* a glycerol molecule bound to the active-site cleft, a (tentative) sodium cation (by analogy with the zymogen structure) and a (tentative) cadmium replacing the catalytic zinc, which was assigned based on electron-density maps, approximate distances to the protein ligands, and its presence in the crystallization conditions. The intermediate MAM domain is less well defined by electron density than the flanking ones, as revealed by a larger average thermal-displacement parameter (123Å^2 *vs.* 109Å^2 and 102Å^2). Despite the lower resolution of the diffraction data, the same asparagine residues as in the zymogen *plus* position 592 showed evident *N*-linked glycosylations, which total 12 *N*-acetylglucosamine, 9 α-D-mannose, 3 α-L-fucose, and 2 β-D-mannose moieties. Therefore, we assume that position 592 is likewise glycosylated in the zymogen but that these sugars are flexible. All four cysteine pairs at adequate distance for disulfide bonding were built as disulfide bridges. Segment 300-310, which contains the C^{305}–mediated intermolecular disulfide bond, was traced based on weak electron density and should be treated with caution. Extra electron density in the active-site cleft was conservatively interpreted as a glycerol molecule.

Miscellaneous — Figures were prepared with program CHIMERA (11). Interaction surfaces (taken as half of the surface area buried at a complex interface) were calculated with CNS (12). Structure similarities were investigated with DALI (13). Model validation was performed with MOLPROBITY (14) and the WHATCHECK routine of WHATIF (15). To obtain a working model for the complete active dimer, a homology model for the EGF-like domain of Mβ (residues 606-647) was constructed with SWISS-MODEL (16) based on a receptor-binding region of Notch ligand (PDB entry 2VJ3; sequence identity 36%; E-value 7.6E-6). This model was connected with constructed models for the transmembrane helix (residues 653-673) and the cytosolic region (674-701), and with the experimental structure

by linkers of stereochemically reasonable conformation. A type-I transmembrane substrate was constructed based on the APP sequence (residues 624-723; UniProt P05067) and the solution structure of Aβ42 in high organic solvent (PDB 1IYT; (17)), keeping its helical conformation only for the transmembrane region. The final coordinates of the experimental structures of human pMβΔC and MβΔC have been deposited with the PDB at www.pdb.org (access codes XXXX and YYYY).

2. ACKNOWLEDGMENTS

We are grateful to the Crystallography Platform (PAC) at IBMB/IRB/PCB for assistance during crystallization experiments. This study was supported in part by grants from European, German, Swiss, Spanish, and Catalan agencies (FP7-HEALTH-F3-2009-223101 "AntiPathoGN"; FP7-HEALTH-2010-261460 "Gums&Joints"; FP7-PEOPLE-2011-ITN-290246 "RAPID"; Deutsche Forschungsgemeinschaft grants DFG Sto185/3-3, BE 4086/1-2, SFB877 (project A9) and German Cluster of Excellence "Inflammation at Interfaces"; Swiss National Science Foundation grant 31003A; BIO2009-10334; BFU2012-32862; CSD2006-00015; a JAE postdoctoral contract from CSIC; Fundació "La Marató de TV3" ref. 2009-100732; and 2009SGR1036). We acknowledge the help provided by EMBL and ESRF synchrotron local contacts. Funding for data collection was provided in part by ESRF.

3. LEGENDS TO THE SUPPLEMENTARY FIGURES

Supplementary Figure S1 — **(A)** Ribbon-type plot of the constituting domains of pMβΔC: PD+CD (ochre and aquamarine; left panel; shown in standard orientation according to (19)), MAM (red; middle panel), and TRAF (purple; right panel). The regular secondary structure elements are labeled (helices α1-α5, strands β1-β30, and 3_{10}-helices η1-η3). The two ions present in the structure, zinc and sodium, are shown as magenta and blue spheres, respectively, as are the cysteine residues (①-⑤). The anchor points of the flexible activation domain are shown by black arrows, and scissors highlight the final maturation cleavage point. **(B)** Topology scheme of the four domains of pMβΔC as in (A). The regular secondary structure elements are depicted, labeled, and their terminal residues indicated. MAM (center) features two intercalated Greek-key motifs (in red and magenta, respectively) and additional elements in pink. TRAF (right) also consists of two intercalated Greek-key motifs (in lilac and purple, respectively) decorated with additional elements in blue. Cysteine residues are shown as yellow sticks and labeled in orange. The seven *N*-glycosylation sites are also shown, with the corresponding asparagine residues labeled in blue. In each case, the most complete sugar structure found in any of the two zymogen molecules or the single mature-enzyme molecule present in the respective crystal asymmetric units is shown; a gray square represents *N*-acetylglucosamine, a circle α-D-mannose, a hexagon β-D-mannose, and a triangle α-L-fucose. See also Sup. Fig. S2. Dashed lines represent regions disordered in the zymogen structure. **(C)** Zinc-binding site environment, with distances: ①, 2.24/2.33Å; ②, 2.06/2.12Å; ③, 2.00/2.06Å; ④, 1.96/1.96Å; and ⑤, 2.13/2.22Å. **(D)** Sodium-binding site, with distances: ①, 2.24/2.37Å; ②,

2.47/2.54Å; ③, 2.21/2.22Å; ④, 2.43/2.47Å; ⑤, 2.87/3.07Å; ⑥, 2.67/2.74Å; and ⑦, 2.51/2.63Å. The two values refer to the two molecules in the crystal asymmetric unit of pMβΔC. Residue E^{268} is not fully defined by electron density.

Supplementary Figure S2 — Scheme depicting the *N*-glycan patterns found in the structure of (p)Mβ. They are in accordance with glycans found in recombinant proteins produced in *Trichoplusia ni* insect cells (see Table 1 in (20)). NAG stands for *N*-acetylglucosamine, MAN for α-D-mannose, BMA for β-D-mannose, and FUC for α-L-fucose. The respective type of glycosidic bond is further shown.

Supplementary Figure S3 — (A) Superposition of the pMβΔC dimer (ochre/aquamarine) onto the active MβΔC dimer (red) in two orthogonal views. The ions correspond to those of the zymogen. **(B)** Superposition in stereo of the CDs of pMβΔC (ochre/aquamarine) and MβΔC (red) in standard orientation (19, 21). **(C)** Close-up view of (B) in stereo displaying the pMβΔC structure and the residues mainly involved in rearrangement upon activation. The segments flanking the disordered activation segment are pinpointed by black arrows. **(D)** Same as (C) for the MβΔC structure.

4. SUPPLEMENTARY REFERENCES

1. Becker C et al. (2003) Differences in the activation mechanism between the alpha and beta subunits of human meprin. *Biol Chem* 384:825-831.
2. Kabsch W (2001) in *International Tables for Crystallography Volume F: Crystallography of Biological Macromolecules*, eds Rossmann MG, Arnold E (Kluwer Academic Publishers (for The International Union of Crystallography), Dordrecht (The Netherlands)), pp 730-734.
3. Evans P (2006) Scaling and assessment of data quality. *Acta Crystallogr sect D* 62:72-82.
4. CCP4 (1994) The CCP4 suite : programs for protein crystallography *Acta Crystallogr sect D* 50:760-763.
5. McCoy AJ et al. (2007) Phaser crystallographic software. *J Appl Crystallogr* 40:658-674.
6. Guevara T et al. (2010) Proenzyme structure and activation of astacin metallopeptidase. *J Biol Chem* 285:13958-13965.
7. Stein N (2008) CHAINSAW: a program for mutating pdb files used as templates in molecular replacement. *J Appl Crystallogr* 41:641-643.
8. Sheldrick GM (2002) Macromolecular phasing with SHELXE. *Z Kristallogr* 217:644-650.
9. Carranza C, Inisan A-G, Mouthuy-Knoops E, Cambillau C, Roussel A (1999) in *AFMB Activity Report 1996-1999* (CNRS-UPR 9039, Marseille), pp 89-90.
10. Blanc E et al. (2004) Refinement of severely incomplete structures with maximum likelihood in BUSTER-TNT. *Acta Crystallogr sect D* 60:2210-2221.
11. Pettersen EF et al. (2004) UCSF Chimera--a visualization system for exploratory research and analysis. *J Comput Chem* 25:1605-1612.

12. Brünger AT et al. (1998) Crystallography & NMR System : a new software suite for macromolecular structure determination *Acta Crystallogr sect D* 54:905-921.
13. Holm L, Kaariainen S, Wilton C, Plewczynski D (2006) Using Dali for structural comparison of proteins. *Curr Protoc Bioinformatics* Chapter 5:Unit 5 5.
14. Davis IW et al. (2007) MolProbity: all-atom contacts and structure validation for proteins and nucleic acids. *Nucl Acids Res* 35 (Web Server issue):W375-W383.
15. Vriend G (1990) WHAT IF : a molecular modelling and drug design program *J Mol Graph* 8:52-56.
16. Arnold K, Bordoli L, Kopp J, Schwede T (2006) The SWISS-MODEL workspace: a web-based environment for protein structure homology modelling. *Bioinformatics* 22:195-201.
17. Crescenzi O et al. (2002) Solution structure of the Alzheimer amyloid β-peptide (1-42) in an apolar microenvironment. Similarity with a virus fusion domain. *Eur J Biochem* 269:5642-5648.
18. Mallorquí-Fernández N et al. (2008) A new autocatalytic activation mechanism for cysteine proteases revealed by *Prevotella intermedia* interpain A. *J Biol Chem* 283:2871-2882.
19. Gomis-Rüth FX, Botelho TO, Bode W (2012) A standard orientation for metallopeptidases. *Biochim Biophys Acta* 1824:157-163.
20. Ailor E et al. (2000) *N*-glycan patterns of human transferrin produced in *Trichoplusia ni* insect cells: effects of mammalian galactosyltransferase. *Glycobiology* 10:837-847.
21. Gomis-Rüth FX, Trillo-Muyo S, Stöcker W (2012) Functional and structural insights into astacin metallopeptidases. *Biol Chem* 393:in press.

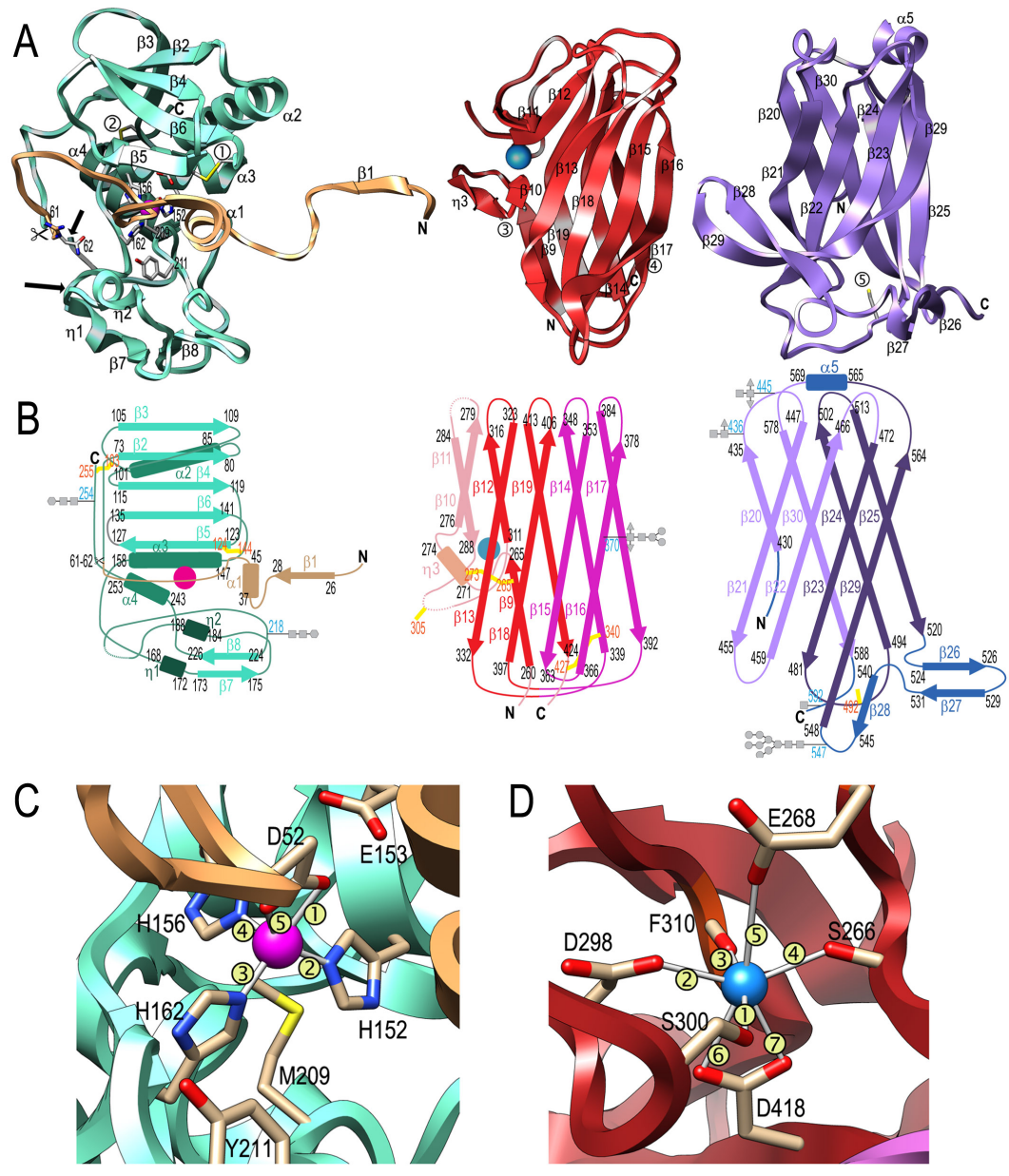
A
B
C
D
D52
E153
H156
H162
H152
M209
Y211
E268
F310
S266
D298
S300
D418

Sup.Fig.S1

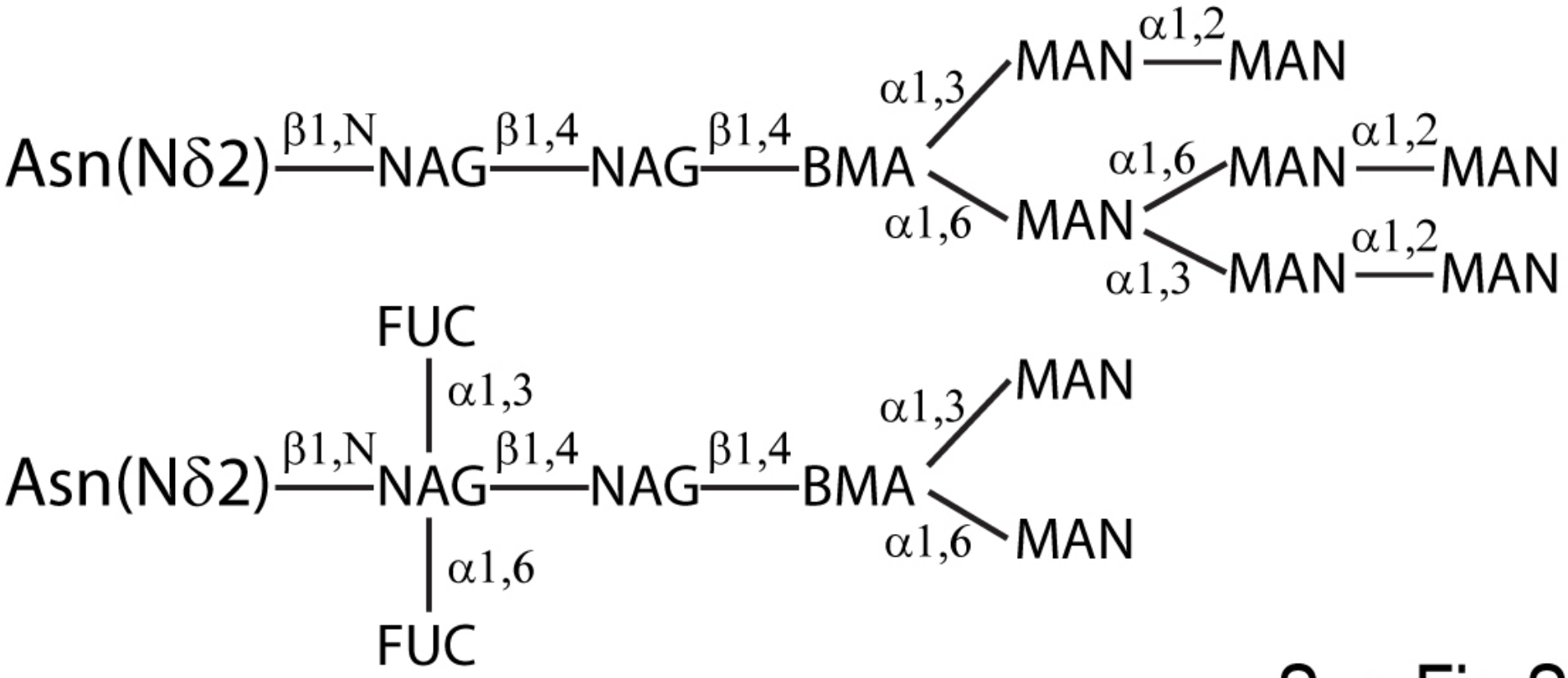
Asn(Nδ2)
β1,N
NAG
β1,4
NAG
β1,4
BMA
α1,3
MAN
α1,2
MAN
α1,6
MAN
α1,2
MAN
α1,6
MAN
α1,3
MAN
α1,2
MAN
FUC
α1,3
Asn(Nδ2)
β1,N
NAG
β1,4
NAG
β1,4
BMA
α1,3
MAN
α1,6
MAN
α1,6
FUC

Sup.Fig.S2

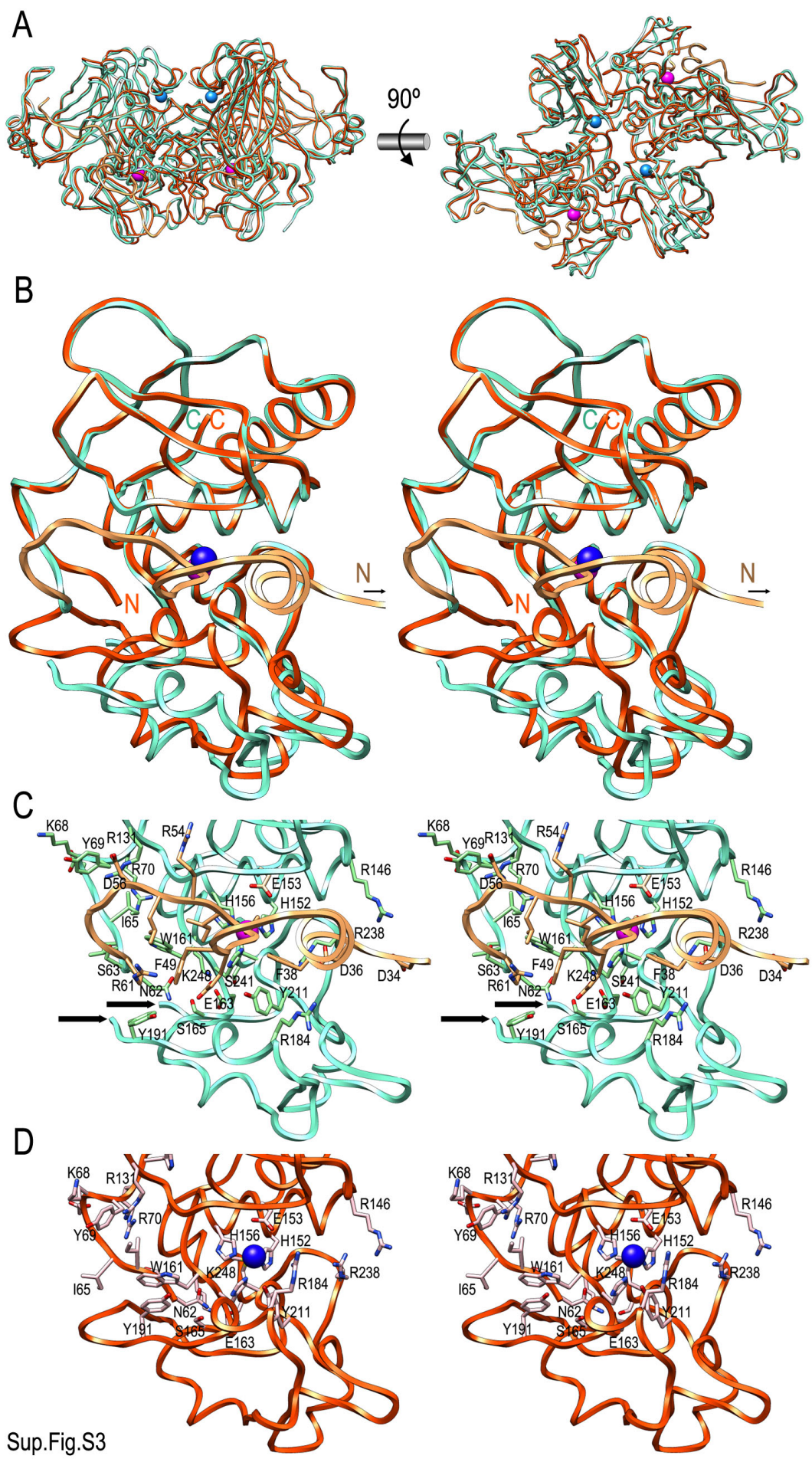
A
90°
B
C
N
C
N
C
N
C
N
C
K68
Y69
R131
R54
R70
D56
E153
R146
H156
H152
I65
W161
R238
S63
F49
K248
S241
F38
D36
D34
R61
N62
E163
Y211
Y191
S165
R184
K68
Y69
R131
R54
R70
D56
E153
R146
H156
H152
I65
W161
R238
S63
F49
K248
S241
F38
D36
D34
R61
N62
E163
Y211
Y191
S165
R184
D
K68
R131
R70
Y69
E153
R146
H156
H152
W161
K248
R184
R238
I65
N62
Y211
Y191
S165
E163
K68
R131
R70
Y69
E153
R146
H156
H152
W161
K248
R184
R238
I65
N62
Y211
Y191
S165
E163

Sup.Fig.S3

SUPPLEMENTARY TABLES

Supplementary Table S1 — Crystallographic data.

Dataset	Pro-meprin β ΔC	Pro-Meprin β ΔC (Zn^{2+}-edge)	Meprin β ΔC (Zn^{2+}-edge)
Space group / cell constants (a, b, c, in Å; α, β, γ in º)	P1 / 69.62, 71.12, 85.74 74.87, 80.08, 65.13	P1 / 69.50,70.70,85.74 74.78, 80.14, 65.25	$P6_122$ / 75.0, 75.0, 502.7 90.0, 90.0, 120.0
Wavelength (Å)	0.9763	1.2815	1.2818
No. of measurements / unique reflections	455,032 / 118,474	351,637 / 91,459	398,689 / 18,106
Resolution range (Å) (outermost shell) [a]	48.45 – 1.85 (1.95 – 1.85)	48.5 – 2.00 (2.11 – 2.00)	48.2 – 3.00 (3.16 – 3.00)
Completeness / Anomalous completeness (%)	96.6 (95.6) / -	94.7 (93.3) / 89.8 (89.7) [d]	99.9 (99.3) / -
R_{merge} [b]	0.069 (0.827)	0.055 (0.494) [d]	0.106 (0.912)
$R_{r.i.m.}$ (= R_{meas}) [b] / $R_{p.i.m.}$ [b]	0.080 (0.959) / 0.041 (0.485)	0.078 (0.699) / 0.055 (0.494) [d]	0.108 (0.932) / 0.022 (0.189)
Average intensity (<[<I> / σ(<I>)]>)	16.6 (2.3)	22.9 (3.4)	22.0 (22.9)
B-Factor (Wilson) ($Å^2$) / Average multiplicity	25.2 / 3.8 (3.9)	27.0 / 3.8 (3.8)	92.2 / 25.1 (3.5)
Resolution range used for refinement (Å)	∞ – 1.85		∞ – 3.00
No. of reflections used (test set)	118,473 (1,124)		17,972 (711)
Crystallographic R_{factor} (free R_{factor}) [b]	0.168 (0.188)		0.196 (0.238)
No. of protein atoms / solvent molecules / ions	8,966 / 808 / 2 Zn^{2+}, 2 Na^+, 5 Cl^-		4,271 / - / 1 Cd^{2+}, 1 Na^+
sugar moieties / ligands	20 NAG, 21 MAN, 8 FUC/ 1 GOL		12 NAG, 11 MAN, 3 FUC/ 1 GOL
Rmsd from target values			
bonds (Å) / angles (°)	0.010 / 0.99		0.008 / 0.98
Aver. B-factors protein / sugars+ligands+waters / ions ($Å^2$)	37.1 / 54.9 / 25.8		110.8 / 146.0 / 104.9
Residue main-chain conformational angle and side-chain rotamer analysis [c]			
favored regions / outliers / all residues / bad rotamers	1,080 / 1 / 1,101 / 2.7%		505 / 1 / 531 / 4.7%

[a] Values in parentheses refer to the outermost resolution shell. [b] For definitions, see Table 1 in (18).
[c] According to MOLPROBITY (14). [d] Friedel pair were treated separately.
NAG, *N*-acetyl glucosamine; MAN, α- or β-mannose; FUC, fucose; GOL, glycerol.